Collinear magnetic structure and multiferroicity in the polar magnet Co_{2}Mo_{3}O_{8}

Y. S. Tang, S. M. Wang, L. Lin, Cheng Li, S. H. Zheng, C. F. Li, J. H. Zhang, Z. B. Yan, X. P. Jiang, and J.-M. Liu

Phys. Rev. B **100**, 134112 — Published 30 October 2019
DOI: 10.1103/PhysRevB.100.134112

Manuscript submitted to Physical Review B (No. BE14223)

Collinear magnetic structure and multiferroicity in polar magnet $Co_2Mo_3O_8$

Y. S. Tang[1], S. M. Wang[1], L. Lin[1],[a)] Cheng Li[2,3], S. H. Zheng[1], C. F. Li[1], J. H. Zhang[1], Z. B. Yan[1], X. P. Jiang[4], and J. –M. Liu [1]

[1]*Laboratory of Solid State Microstructures, Nanjing University, Nanjing 210093, China*

[2]*Forschungszentrum Jülich GmbH, Jülich Centre for Neutron Science Outstation at SNS, Germany*

[3]*Oak Ridge National Laboratory, Oak Ridge, TN 37831, USA*

[4]*School of Materials Science and Engineering, Jingdezhen Ceramic Institute, Jingdezhen 333403, China*

[a)] Corresponding author, Email: llin@nju.edu.cn

[**Abstract**] Among numerous multiferroic phenomena observed in spin frustrated lattice, giant magnetoelectricity in honeycomb lattice (Fe, Mn)$_2$Mo$_3$O$_8$ has stimulated great interest and substantial effort in searching for novel members in this 238 family. In this work, we synthesize successfully compound Co$_2$Mo$_3$O$_8$, a structural analogue of Fe$_2$Mo$_3$O$_8$, and present a series of characterizations on its structural, magnetic, and electric properties. An antiferromagnetic transition takes place at the Neel temperature $T_N = 39$ K with appearance of electric polarization and dielectric anomaly, which provides clear evidence of simultaneous magnetic and ferroelectric transitions. The neutron powder diffraction (NPD) and magnetic susceptibility data confirm the *c*-axis collinear antiferromagnetic orders and emergent ferroelectric polarization. In particular, such antiferromagnetic order is relatively robust against magnetic field up to 9 T, different from Fe$_2$Mo$_3$O$_8$ with ferrimagnetic transition or Mn$_2$Mo$_3$O$_8$ with spin flop in the low-field region. Our data on single crystals demonstrate the second-order magnetoelectric effect in terms of magnetic field dependence of ferroelectric polarization response, while no linear magnetoelectric response is allowed. It is suggested that Co$_2$Mo$_3$O$_8$ provides a unique platform on which rich multiferroic physics in the presence of collinear magnetic order can be explored.

I. Introduction

Multiferroic materials exhibiting more than one primary ferroic order in a single phase have driven significant research activity [1, 2]. The mutual control and coupling between these ferroic orders, especially magnetoelectric (ME) coupling between magnetization (*M*) and ferroelectric polarization (*P*), offer new routes to device architectures [3-7]. From the fundamental point of view, it is highly concerned that some noncollinear antiferromagnetic (AFM) ordering may lead to the inversion symmetry breaking, as evidenced in a number of so-called type II multiferroics (spin order driven ferroelectricity). Nevertheless, in these compounds, the ferroelectric Curie temperature and ME signal are seriously limited [8-11]. In spite of great improvement in understanding the ME effect in such compounds, searching for room-temperature multiferroic candidates and colossal ME effect has been difficult, hindering device applications.

Along this line, one class of promising candidates includes those systems with linear ME effects, in which the remarkable tunability of ME coefficients is achieved by chemical modification [12-15]. Recent breakthroughs in $Fe_2Mo_3O_8$ [12, 16-19], $Co_4Nb_2O_9$ [20], $CaBaCo_4O_7$ [21], $GaFeO_3$ [22], and Ni_3TeO_6 [23] have stimulated a flurry of research on these new multiferroics. Among them, the family of $A_2Mo_3O_8$ (A = Fe, Mn, Co and Ni) belongs to the non-centrosymmetric space group $P6_3mc$ with A^{2+} ions occupying both the octahedral (OCT) and tetrahedral (TET) sites, as shown in Fig. 1(a). The crystal structure can be viewed as the stacking of honeycomb-like $A_2O_8^{12-}$ layers and sheets of Mo^{4+} ions along the *c*-axis. Here the Mo^{4+} ions form the unique spin-singlet trimers, and do not contribute to magnetism [24]. The spin frustration inherent to such honeycomb lattice arises due to the competing long-range magnetic interactions and anisotropic magnetic exchanges. Therefore, the magnetic properties of this family are different from one and another [25, 26], as exampled by Fig. 1(b) & (c) where the collinear AFM order of $Fe_2Mo_3O_8$ and ferrimagnetic (FIM) order of $Mn_2Mo_3O_8$ by taking into account the Mn/Fe - O coordination are illustrated.

Recently, large linear ME coupling reported in $Fe_2Mo_3O_8$ [12, 16] triggered more efforts in the search for large linear ME systems. An interesting feature of $Fe_2Mo_3O_8$ is the tunability between the distinct magnetic ground states by Zn-doping, which leads to the varied ME coefficient from -142 ps/m to 107 ps/m [12]. Similar linear ME susceptibility was also observed in $Mn_2Mo_3O_8$, and large manipulation of ME coefficient by Fe-doping was found [17]. These emergent effects suggest that the $A_2Mo_3O_8$ family is a rich source for large linear ME effects and indeed a number of works regarding this issue have been reported [18, 19]. It is also interested to check for species substitution because different *d*-orbital filling strategies make the magnetic and ME properties of this family distinctly different. It was suggested that the non-filling of 3*d* orbitals of the A ions and strong magnetic anisotropy govern the Neel temperature (T_N): T_N = 59.5 K, 41.5 K, 40.8 K, and 6 K for A^{2+} = Fe^{2+} (S = 2), Mn^{2+} (S = 5/2), Co^{2+} (S = 3/2), and Ni^{2+} (S = 1), respectively [27, 28]. One case is $Ni_2Mo_3O_8$, which was previously reported to remain paramagnetic until T = 2 K [27] whereas an AFM ordering with a mixture of stripy and zigzag character was discovered most recently [28]. Nonetheless, little about the $3d^7$ Co^{2+} isotype oxides has been known, a mystery exception.

The first-principles calculations show that exchange striction is the leading mechanism responsible for the observed ME effects in $Fe_2Mo_3O_8$ [16]. It was suggested that the ground state allows the oxygen ion displacement so that the magnetic energy gains in the AFM and FIM states is maximized, illuminating the underlying mechanism for the observed giant ME coefficients. However, so far, no direct experimental evidence has been presented and all these claims are based on theoretical predictions. Despites powder neutron scattering of $A_2Mo_3O_8$ compounds where A = Mn, Fe, Co, or 1/2(Fe_xZn_{2-x}) was performed as early as the 1970s [29], the ground magnetic structures of these compounds were proposed based on data with narrow *d*-value range, without detailed atom positions due to the low resolution of the data [27]. Furthermore, investigation of lattice phase transition is still missing. Therefore, systematic neutron scattering investigations on these compounds are highly desired to unveil the ME mechanism.

Motivated by these facts, we here report an investigation of dielectric, ferroelectric, ME coupling, magnetic order, and specific heat of polycrystalline and single crystal $Co_2Mo_3O_8$, one member of the $A_2Mo_3O_8$ family. An AFM transition at T_N = 39 K, accompanied with a dielectric anomaly and a jump in electric polarization is revealed, which provides a clear evidence for simultaneous magnetic and ferroelectric transitions. Furthermore, a magnetic field - induced suppression of the electric polarization and a shifting of the ferroelectric Curie temperature (T_{FE}) below T_N is identified. To more precisely capture the intrinsic physics, measurement on single crystals reveals that ferroelectric polarization is indeed aligned along the *c*-axis, and nonlinear ME coupling effect (P is quadratic to magnetic field H) is also evidenced, which is distinct from that identified in $Fe_2Mo_3O_8$ and $Mn_2Mo_3O_8$. The neutron scattering data suggest a layered collinear AFM magnetic structure along the *c*-axis, and detailed ions displacement upon transition from PM to AFM state are explicitly obtained. All these results point towards $Co_2Mo_3O_8$ as a new and unusual multiferroic member in this $A_2Mo_3O_8$ family.

II. Experimental details

The polycrystalline $Co_2Mo_3O_8$ samples were synthetized by the standard solid-state reaction method [30, 31]. The sintering procedure has been optimized by repeated experiments. Stoichiometric amounts of CoO and MoO_2 powder were ground with a molar ratio 2:3 in an agator mortar, and sealed in evacuated silica tubes at 1000 ^{o}C for 48 h. The obtained power was compressed into a rod under hydrostatic pressure, and heated at 600 ^{o}C for 40 min under a pressure of 5.0 GPa. Then the rod was cut into plates, and each plate was polished into a thin disk of ~ 3.0 mm in diameter and ~ 0.2 mm in thickness. Sufficient plates were again broken into a large amount of powder for subsequent neutron scattering experiments. The single crystals were grown by chemical vapor transport reaction method as described in [27].

The crystallinity of the as-prepared samples was checked using X-ray diffraction (XRD, D8 Advanced, Bruker) in the θ - 2θ mode with Cu K_α source (λ = 1.5406 Å). The neutron powder diffraction (NPD) experiment was performed on the BL-11A powder diffractometer at the Oak Ridge National Laboratory. Approximately 4.93 g powder was loaded into an 8 mm Vanadium can, which was then backfilled with Helium before the loading. The data were collected using POWGEN auto changer in the high-resolution mode, with a center wavelength of 1.5 Å. Approximately 2 hours gathering time was used for each temperature (300 K, 50 K and 10 K). The crystal and magnetic structures were refined using the TOPAS v5 and JANA 2006 software [32, 33].

The *dc* magnetization was measured using the Quantum Design superconducting quantum interference device magnetometer (SQUID) with a measuring magnetic field of 1000 Oe in the zero field-cooling (ZFC) mode and field-cooling (FC) mode. At the same time, the specific heat (C_P) was measured using the Quantum Design Physical Property measurement system (PPMS) in the standard procedure.

For the electrical measurements, each of the disk-like samples was coated with the bottom and top Au electrodes for dielectric and ferroelectric probing. The dielectric constant (ε) as a function of temperature (T) was measured using the HP4294A impedance analyzer integrated with PPMS. For the spontaneous polarization P, the pyroelectric current method was used in the standard mode, as described in Ref. [34]. The pyroelectric current I_{py} in the warming sequence with the sample warming rate of 2, 4 and 6 K/min was collected using Keithely 6517 programmable electrometer.

III. Results and discussion

A. Magnetization and specific heat

The T dependence of magnetic susceptibility $\chi(T)$ curves with the measuring magnetic field of 1000 Oe under the ZFC and FC modes are plotted Fig. 2(a). In agreement with previous results, $\chi(T)$ shows a cusp at $T_N \sim 39$ K, suggesting the antiferromagnetic ordering. In addition, the Curie-Weiss law fitting of the inverse magnetic susceptibility above 40 K yields the Weiss temperature $\theta_{cw} \sim -138.9$ K, indicative of strong antiferromagnetic interactions. The effective paramagnetic magnetic moment $\mu_{eff} = 4.250$ μ_B/Co is derived, close to the expected spin-only moment of 3.873 μ_B/Co for high spin Co^{2+} ($S = 3/2$).

Here, it should be pointed out that a small tip in addition to the relatively broad bump-like peak around T_N in the $\chi(T)$ curve can be seen. Such a small tip remains to be an issue although it was also observed in some earlier experiment [27] where the measured χ on single crystals for the $H\perp c$ mode exhibited such a small tip but no such tip in the $H//c$ mode can be seen. It is reasonable to understand the different details in the magnetic susceptibility near T_N between different samples. Of course, there may be other possibilities, e.g. ferromagnetic impurities, which are difficult to be distinguished by conventional XRD actually, and even by neutron measurement (only tiny amount of MoO_2 impurity phase was found). As species Fe is often an impurity in the Co-based samples, the small peak near the magnetic transition might be attributed to the impurity effect as reported in $Co_{1/3}TaS_2$ [35]. Nevertheless, no clear evidence with this guess is available while this feature does not affect the subsequent determination of magnetic structure as well as ME response measurement.

In Fig. 2(b), we plot the magnetic field (H) dependent magnetization (M) under several selected temperatures (T). The magnetization increases monotonically with H, a typical AFM feature. No field-induced magnetic transition or spin flop has been observed up to H = 9 T, implying that $Co_2Mo_3O_8$ slightly differs from other members of this 238 family. Certainly, it is expected that such a transition would occur if higher magnetic field is applied, and it is highly desirable to measure the ultra-field data (e.g. 50 T) to unveil the possible magnetic transition in $Co_2Mo_3O_8$. Unfortunately, such a measurement is not accessible to us but its absence does not change the main conclusion we shall reach.

Subsequently, we switch our attention to the specific heat C_P. A large anomaly in the specific heat is present at the magnetic transition point, as seen in Fig. 3(a). To uncover the magnetic contribution to the specific heat, we measured the specific heat of nonmagnetic compound $Zn_2Mo_3O_8$, structurally analogous to $Co_2Mo_3O_8$. The magnetic contribution C_M as a function of T can be approximated by subtracting the value of $Zn_2Mo_3O_8$ (phonon term). One sees clearly an enhancement of the specific heat occurring at T_N, is ~ 30 J mol^{-1} K^{-1}, which can be seen as the magnetic contribution term to the specific heat, i.e. C_M. This term is smaller than the value deduced from the mean-field theory. As the first-order approximation, we assume that all the Co^{2+} ions are in the high-spin (S = 3/2) state. The magnetic contribution C_M can be written as:

$$C_M = 5R\frac{2S(S+1)}{S^2+(S+1)^2} \sim 36.7 \text{ J mol}^{-1} \text{ K}^{-1}, \tag{1}$$

where R is the gas constant. Here, the slight difference between the measured value and evaluated value from Eq. (1) suggests the presence of short-range magnetic correlation at higher temperature in $Co_2Mo_3O_8$. Besides, the measured C_M data at low temperature is well fitted with the power law $C_M \sim T^3$, which is consistent with the power-law expression for a three-dimensional antiferromagnet [36].

The T dependence of magnetic entropy $\Delta S_M(T)$ is also shown in Fig. 3(b). Strikingly, the entropy loss occurs at T_N with a saturation value ΔS_M (T = 50 K) ~ 11.50 J mol^{-1} K^{-1}, just half of the saturated value. This phenomenon is similar to recent reports on sister-compounds $Fe_2Mo_3O_8$ and $Ni_2Mo_3O_8$ [16, 28]. It is worthwhile to point out that application of magnetic field up to 9 T does not cause obvious peak shifts as shown in Fig. 3(c), suggesting a robust antiferromagnetic coupling, coincident with the magnetization behaviors.

B. Magnetic structure determination

The NPD data were collected at T = 300 K, 50 K and 10 K, and the Rietveld refinement results are presented in Fig. 4. About 2.4 wt% of MoO_2 impurity phase was found in the sample, therefore the Mo occupancy was initially released. However, the refined value does not differ from the stoichiometric compound, and thus the occupancy of Mo site is fixed for the subsequent refinement. At room temperature, the refined structure of $Co_2Mo_3O_8$ exhibits the non-centrosymmetric $P6_3mc$ space group with unit cell parameters $a = b$ = 5.7698(1) Å, and c = 9.9134(1) Å, well consistent with earlier reported data [27]. The detailed refined atomic parameters at 300 K and 10 K are given in Table I and Table II, respectively. These data allow us to discuss the magnetic structure of $Co_2Mo_3O_8$.

It is noted that earlier investigation of magnetic ordering in $A_2Mo_3O_8$ systems was pioneered by McAlister and Strobel [27, 30]. Most recently, Morey *et al.* reported the magnetic structure of $Ni_2Mo_3O_8$ at T = 1.6 K and found that the doubling along the *ab*-plane with wave vector $\boldsymbol{k}$ = (1/2, 0, 0) is required to fully index the magnetic reflections [28].

Consequently, a quite complex magnetic ordering, consisting of the stripy *ab*-plane moment and zigzag AFM ordering along the *c*-axis was reported. When it comes to $Co_2Mo_3O_8$, we first identify the magnetic Bragg peaks by subtracting the neutron powder diffraction pattern measured at $T > T_N$ from that at $T < T_N$, as shown in the inset of Fig. 4(c). The highest magnetic peak is located at $Q \sim 0.792$ Å^{-1}. At $T = 10$ K, all the magnetic reflections could be indexed using the nuclear cell, and thus a search for the magnetic structure with $\boldsymbol{k} = (0, 0, 0)$ was conducted using the ISODISTORT package [37]. Choosing the Wycoff position of Co, 2*b*, as the magnetic sites, the search returns four Irreducible Representations (IRs) that have a single order parameter direction (OPD), namely mGM2, mGM3, mGM5 and mGM6, and contain eight magnetic space groups (S.G.), listed in Table III. Previous magnetic measurement identified the *c*-axis as the easy axis for AFM ordering [31], and thus we focus on the space groups that produce the AFM ordering along the *c*-axis. Here, the "+" or "–" signs denote the direction of magnetic moment along *c* at the tetrahedral (T) and octahedral (O) sites, in the adjacent chain in the order of TTOO.

In our fitting, all the six space groups were tested, and the + − + − configuration in general produces better fitting results than the + + − − sets: an improved fitting with $R_{wp} = 7.1\%$ to $R_{wp} = 5.1\%$ was obtained if one switches from S.G. 186.207 to 186.205. However, lowering the symmetry to S.G. 36.174 to include the in-plane contribution leads to a minor improvement in the fitting quality ($R_{\mathrm{wp}} = 5.0\%$), which is not sufficient strong to support the existence of *ab*-plane moment. Therefore, the S.G. 186.205 is considered an accurate depiction of the magnetic structure. Finally the refined magnetic structure exhibits the Ising-type AFM order along the *c*-axis (see Fig. 5), the same as that in $Fe_2Mo_3O_8$.

It is worth noting that the refined moments on the tetrahedral and octahedral sites are highly correlated and the refined moment was 3.44(1) μ_B for Co1, and 3.35(1) μ_B for Co2 site, respectively. In $Fe_2Mo_3O_8$, the octahedral site of Fe (Fe_o) has larger spin than the tetrahedral site (Fe_t) with the magnitude of moment 4.21 μ_B and 4.83 μ_B. Thus the comparable difference between Fe_o and Fe_t results in the ferrimagnetic transition with application of magnetic field. Therefore, the magnetic order of $Co_2Mo_3O_8$ is essentially different from that identified for

$Fe_2Mo_3O_8$ and $Mn_2Mo_3O_8$, and thus different response to magnetic field, namely no ferrimagnetic transition or spin flop, is rationalized in $Co_2Mo_3O_8$, as shown in the M - H data. From this point of view, it is highly recommended to further explore the ferroelectricity and possible ME coupling underneath the collinear magnetic order in $Co_2Mo_3O_8$, to be discussed below.

C. Dielectric, ferroelectric, and multiferroic properties

Along this line, we first discuss the dielectric response as a function of T. The measured dielectric constant $\varepsilon(T)$ at several frequencies are plotted in Fig. 6(a). Clearly, these curves reveal an anomaly occurring at $T \sim T_N$, indicating the simultaneous magnetic and structural transitions. In particular, the anomaly is somehow frequency independent, but the peak strength is frequency dependent, indicating that this dielectric anomaly is related to the spin-induced ferroelectric phase transition rather than from relaxation [38-40]. However, the $\varepsilon(T)$ data at a fixed frequency shift upward with increasing magnetic field and the dielectric anomaly also shifts towards the high-T side as shown in Fig. 6(b). These behaviors are understandable since the dielectric anomaly is associated with the magnetic transition at T_N and the magnetic field enhances ferromagnetic correlation in $Co_2Mo_3O_8$.

We then investigate the ferroelectricity and magnetoelectric response of $Co_2Mo_3O_8$ by probing the pyroelectric current, to probe magnetism-induced ferroelectrics. Given that the lattice structure is polar, it is more interested to investigate the magnetic-induced polarization. Therefore, the pyroelectric current $I_{py}(T)$ on the sample upon cooling from $T = 60$ K to $T = 2$ K under a poling electric field of 10 kV/cm was measured under magnetic field strength from 0 T to 6 T (note that $T_N \sim 40$ K). This scheme ensures that the measured $I_{py}(T)$ is purely magnetically generated and the integration of $I_{py}(T)$ data from the high-T side corresponds to a variation of polarization. Here, we still used P for characterizing the ferroelectric polarization to distinguish the variation of polarization (ΔP) vs. ramping magnetic field.

We first look at the $I_{py}(T)$ curves measured at three different warming rates at 2, 4 and 6 K/min to verify the reliability of our methodology. No distinct shifting of the $I_{py}(T)$ peaks is observed, and the polarization was reversed by applying a reverse voltage, as shown in Fig. 7(a) and the inset, suggesting that the detected current does come from the pyroelectric effect. The data revealed the simultaneous magnetic ordering and appearance of ferroelectric polarization. The saturated value of P in the low-T side is ~ 40 μC/m^2, much smaller than the values observed in single crystals $Fe_2Mo_3O_8$ (~ 1400 μC/m^2) and $Mn_2Mo_3O_8$ (~ 2000 μC/m^2). This difference is ascribed to the sample nature, noting that the measured polarization in polycrystalline samples is usually much smaller than that in single crystals for multiferroics. We shall return to this issue below when we discuss the ferroelectric polarization direction from our preliminary data on single crystal samples.

The most important issue is the linear ME (LME) effect to be checked for $Co_2Mo_3O_8$. We employed two modes to check the ME effect. First, we collected the $I_{py}(T)$ data under a constant magnetic field H, as plotted in Fig.7(b). It can be found that the peak height has only weak shift downwards with increasing H, and a shifting of the ferroelectric Curie temperature (T_{FE}) below T_N is identified, suggesting weak suppression of ferroelectric polarization by magnetic field. The as-evaluated $P(T)$ curves under these H values are shown in Fig. 7(c), indicating that the polarization suppression is indeed minor if any. Second, we also measured the isothermal magnetoelectric current as a function of H during the H-cycling between 5.0 T and -5.0 T. Our measurements failed to observe remarkable ME response as shown in Fig. 7(d), and the detected current was on the similar level as the background current noise ~ 0.1 pA. We shall come back to this issue once more below.

Due to the polycrystalline nature of the samples, the ME coupling measured in these samples is often elusive, and might escape detection if the signal is intrinsically low, or if the magnetic energy gain is not sufficient to overcome the energy barrier between multiple grains. From such perspective, single crystal is much more favorable to investigate the underlying multiferroic property. While the ME effect in this system is one of the core issues addressed in this work, substantial effort has been made to synthesize single crystal samples. In spite of challenges, we eventually grew successfully some very small single crystal plates. Fortunately, these small crystals allow us to perform some additional measurements on the c-axis ferroelectric polarization if any.

The slow-scan XRD pattern focusing on the naturally developed hexagonal plane is plotted in Fig. 8. Comparing with the standard XRD diffraction pattern, the plane is well indexed by (00l). In addition, the crystal was aligned by Back-Reflection Laue Detector (The MWL120, Multiwire Laboratories, Ltd.), and this hexagonal plane shows perfect diffraction spots from the [001] direction (Fig. 8 inset), and no other sets of spots are found, demonstrating good quality of our crystal. Here we note that our as-grown crystals are basically with diameter of ~ 0.5 mm and thickness of 10 - 100 μm as shown in the inset, that it is difficult to cut a piece of *ab*-plane to conduct the electric measurement owing to the small thickness. Therefore, only the ferroelectric polarization along the *c*-axis will be discussed below. To probe the ME effect, the magnetoelectric current (I_c) along the *c*-axis was measured at ramping magnetic field with 100 Oe/s by the scan from + H to - H, and then - H back to + H, forming a swamping cycle.

Fig. 9(a) displays the pyroelectric current I_c and electric polarization P_c as a function of T. In contrast to the data from polycrystalline samples, the I_c data here show rapid increasing near the transition point T_N, and then slowly decreases with further decreasing T, and finally drops down to zero below 15 K. The I_c variation near T_N is noticeably sharper than that in polycrystalline samples. In addition, as we have claimed earlier, the magnitude of polarization in single crystals is indeed much larger (~ 1160 μC/m^2 at T = 2 K) than that in polycrystalline samples (40 μC/m^2). This value is still smaller than but comparable on the order of magnitude with the polarizations observed in $Fe_2Mo_3O_8$ and $Mn_2Mo_3O_8$, implying that the as-grown crystals, in spite of very small in size, may be useful for unveiling some issues uncovered in polycrystalline samples.

First, to explore the possible ME effect stemming from the collinear spin order, we examined the T dependence of magnetic susceptibility in the $H//c$ and $H\perp c$ geometries, and found the same behaviors as previously reported by Mcalister et al [27] (not shown here). Here we present the H dependence of M the two modes, measured at T = 5 K in Fig. 9(b). Clearly, the M - H data along the two different crystallographic directions suggest absence of any magnetic transition or spin flop below $H = 9$ T, as observed in polycrystalline samples. In particular, the linear increase of magnetization vs. field bears some resemblance to the response of polarization in the $H//c$ mode, as shown in Fig. 9(c). The term of magnetic field driven polarization, ΔP_c, as a function of H, is obtained by scanning from + H to - H, and then from - H back to + H. In the low-T range, ΔP_c remains nearly the same, and then increases quickly at $T \sim 30$ K up to ~ 9 times larger than that at $T = 2$ K, keeping in mind that the largest variation of ΔP_c in $Fe_2Mo_3O_8$ also appears at intermediate T range, e.g., $T = 45$ K [12].

In addition, it is worth noting that all the ME effect and M - H curves were measured in the relatively low field range ($H \leq 9$ T). It is suggested that magnetic transition and inherent ME response in the ultrahigh magnetic field range, e.g. up to 50 T, cannot be neglected. These high magnetic field measurements would be useful for revealing the spin dynamics in $Co_2Mo_3O_8$, which is beyond the scope of this work and unfortunately not accessible at this moment.

Second, one is allowed to formulate the ME response from the phenomenological viewpoint and discuss the relevant microscopic mechanisms associated with the magnetic point group $6_3'm'c$. In general, ΔP is given as a function of H up to the second order as follows:

$$\Delta P = P_c + P_s + \alpha H + \beta H^2, \tag{2}$$

where P_c and P_s are the crystallographic and spin-induced spontaneous polarization, which are finite even under zero field [17]. The coefficients α and β correspond to the first-order and second-order ME coefficients, respectively. Here, we exemplify the ΔP_c - H curves measured at $T = 30$ K in the $H//c$ mode and the fitting is plotted as dashed lines in Fig. 9(c). It is clearly seen that the data shows perfect fitting by introducing the second-order ME term. The ΔP_c term is quadratic to H with the second-order ME coefficient $\beta = 29.59 \times 10^{-19}$ s/A in the $H//c$ mode. This result is consistent with the fact that the magnetic space group for the antiferromagnetic order ($P6_3'm'c$) allows only the second-order ME effect, while the linear ME effect is forbidden.

Nonetheless, these results contrast to the previous ME coefficients in $Fe_2Mo_3O_8$ and

$Mn_2Mo_3O_8$, in which the linear ME coupling plays an important role. In particular, the second-order ME susceptibility β of $Co_2Mo_3O_8$ is considerably larger than that of $Fe_2Mo_3O_8$ (1.81×10^{-28} s/A) which manifests the same magnetic ground state [12]. Therefore, $Co_2Mo_3O_8$ seems to be a peculiar new multiferroic member that is distinctly different from the other two well recognized linear magnetoelectric members in this 238 family.

D. Ionic displacement

Finally, we would like to discuss the possible structural distortion associated with the magnetic transition at T_N from the macroscopic point of view based on the NPD data. To evaluate the distortion, we need to extract the ionic coordinates of the lattice unit from the structural fitting so that the ionic displacements can be obtained. In proceeding, the lattice structure was expanded to be commensurate with the magnetic cell (Space group $P6_3$'m'c, 186.205). Overall, minor change in the nuclear structure was found after the transition. Nevertheless, we can obtain the ionic displacement for each ion associated with the paramagnetic (PM) to AFM transition at T_N, while the nuclear structure in the original space group ($P6_3mc$, S.G. 186) is kept.

We then compare the structure parameter between the 50 K and 10 K data by using the same S.G. ($P6_3mc$). Based on the symmetry operation, all the displacements along x and y will be canceled out, and the ionic shifts along c directions during the paramagnetic to AFM transition are obtained. In fact, symmetry operations of the space group limit the ferroelectric polarization to align with the c-axis, whereas the in-plane polarization component is not allowed [41].

For the 238 family, it is well recognized that the exchange striction, where the lattice deforms to gain the exchange energy, contributes to the ferroelectric polarization. The first principle calculations demonstrate that the main ionic shift comes from O3 and O4 as schematically illustrated in Fig. 10 [16]. The Fe-O-Fe angle (θ) between the nearest Fe^{2+} increases from 109° to $\sim 111^{\circ}$ upon the transition from the PM to the AFM state due to the oxygen shifts. Hence, we believe that the exchange striction should equally apply to

$Co_2Mo_3O_8$, taking the collinear magnetic order into account. However, it is surprised that the Co-O-Co angle is essentially unchanged at all for the $Co_2Mo_3O_8$ case as shown in Fig. 10, in which all the ionic displacements are illustrated. The main displacement comes from Co1 and O2, and Co2 ions are nearly unchanged, while displacements of Fe1 and Fe2 ions in $Fe_2Mo_3O_8$ are comparative in the PM to AFM states according to the calculations.

IV. Conclusion

In conclusion, we have systematically investigated the magnetic structure and multiferroic property in polar antiferromagnet $Co_2Mo_3O_8$. The antiferromagnetic moment and associated ferroelectric polarization generation along the *c*-axis are well evidenced by neutron scattering. Remarkable ME coupling has been observed in the single crystals but very weak in the polycrystalline samples. The previously recognized linear magnetoelectric effect in other members of this 238 family is not observed in $Co_2Mo_3O_8$, suggesting some specific characteristics with this system. More importantly, the second-order ME coupling, which is stronger than those observed in $Fe_2Mo_3O_8$ is significant for $Co_2Mo_3O_8$. In particular, the antiferromagnetic order remains relatively robust against magnetic field up to 9 T, making it distinctive among this 238 multiferroic family. The neutron scattering data suggest the collective displacement of Co1 and O2 ions to gain the exchange energy, giving rise to the *c*-axis ferroelectric polarization. Further ultra-high magnetic field measurements would be highly required to quantify possible magnetic transition to unveil the hidden magnetic order as well as the inherent ME coupling in $Co_2Mo_3O_8$.

ACKNOWLEDGMENTS

This work was financially supported by the National Key Research Program of China (Grants No. 2016YFA0300101) and the National Science Foundation of China (Grants No. 11874031, 11834002, 11774106, 51431006, 51721001 and 11974167). A portion of this research used resources at Spallation Neutron Source, a DOE Office of Science User Facility operated by the Oak Ridge National Laboratory.

References

1. S.-W. Cheong, and M. Mostovoy, Multiferroics: a magnetic twist for ferroelectricity. Nat. Mater. **6**, 13 (2007).
2. S. Dong, J.-M. Liu, S.-W. Cheong, and Z. Ren, Multiferroic materials and magnetoelectric physics: symmetry, entanglement, excitation, and topology. Adv. Phys. **64**, 519 (2015).
3. S.-W. Cheong, D. Talbayev, V. Kiryukhin, and A. Saxena, Broken symmetries, non-reciprocity, and multiferroicity, npj Quant. Mater. **3**, 19 (2018).
4. C. L. Lu, M. H. Wu, L. Lin, and J.-M. Liu, Single-phase multiferroics: new materials, phenomena, and physics, Natl. Sci. Rev. **6**, 653 (2019).
5. K. Xu, X. Z. Lu, and H. J. Xiang, Designing new ferroelectrics with a general strategy, npj Quant. Mater. **2**, 1 (2017).
6. C. L. Lu and J.-M. Liu, $DyMnO_3$: A model system of Type-II multiferroics, J. Materiomics **2**, 213 (2016).
7. S. Dong, H. J. Xiang, and E. Dagotto, Magnetoelectricity in multiferroics: a theoretical perspective, Natl. Sci. Rev. **6**, 629 (2019).
8. Y. J. Choi, J. Okamoto, D. J. Huang, K. S. Chao, H. J. Lin, C. T. Chen, M. van Veenendaal, T. A. Kaplan, and S.-W. Cheong, Thermally or magnetically induced polarization reversal in the multiferroic $CoCr_2O_4$, Phys. Rev. Lett. **102**, 067601 (2009).
9. R. D. Johnson, L. C. Chapon, D. D. Khalyavin, P. Manuel, P. G. Radaelli, and C. Martin, Giant improper ferroelectricity in the ferroaxial magnet $CaMn_7O_{12}$, Phys. Rev. Lett. **108**, 067201 (2012).
10. M. Kenzelmann, G. Lawes, A. B. Harris, G. Gasparovic, C. Broholm, A. P. Ramirez, G. A. Jorge, M. Jaime, S. Park, Q. Huang, A. Ya. Shapiro, and L. A. Demianets, Direct transition

from a disordered to a multiferroic phase on a triangular lattice, Phys. Rev. Lett. **98**, 267205 (2007).

11. K. Taniguchi, N. Abe, T. Takenobu, Y. Iwasa, and T. Arima, Ferroelectric Polarization Flop in a Frustrated Magnet $MnWO_4$ Induced by a Magnetic Field, Phys. Rev. Lett. **97**, 097203 (2006).
12. T. Kurumaji, S. Ishiwata, and Y. Tokura, Doping-Tunable Ferrimagnetic Phase with Large Linear Magnetoelectric Effect in a Polar Magnet $Fe_2Mo_3O_8$, Phys. Rev. X. **5**, 031034 (2015).
13. Michael J. Pitcher, Pranab Mandal, Matthew S. Dyer, Jonathan Alaria, Pavel Borisov, Hongjun Niu, John B. Claridge and Matthew J. Rosseinsky, Tilt engineering of spontaneous polarization and magnetization above 300 K in a bulk layered perovskite, Science **347**, 420 (2015).
14. K. Du, B. Gao, Y. Z. Wang, X. H Xu, J. W. Kim, R. W. Hu, F.-T. Huang, and S.-W. Cheong, Vortex ferroelectric domains, large-loop weak ferromagnetic domains, and their decoupling in hexagonal (Lu, Sc)FeO_3, npj Quant. Mater. **3**, 33 (2018).
15. M. Morin, E. Canévet, A. Raynaud, M. Bartkowiak, D. Sheptyakov, V. Ban, M. Kenzelmann, E. Pomjakushina, K. Conder, and M. Medarde, Tuning magnetic spirals beyond room temperature with chemical disorder, Nat. Commun. **7**, 13758 (2016).
16. Y. Z. Wang, G. L. Pascut, B. Gao, T. A. Tyson, K. Haule, V. Kiryukhin and S.-W. Cheong, Unveiling hidden ferrimagnetism and giant magnetoelectricity in polar magnet $Fe_2Mo_3O_8$, Sci. Rep. **5**, 12268 (2015).
17. T. Kurumaji, S. Ishiwata, and Y. Tokura, Diagonal magnetoelectric susceptibility and effect of Fe doping in the polar ferrimagnet $Mn_2Mo_3O_8$, Phys. Rev. B **95**, 045142 (2017).
18. S. K. Yu, B. Gao, J. W. Kim, S.-W. Cheong, M. K. L. Man, J. Madéo, K. M. Dani, and D. Talbayev, High-Temperature Terahertz Optical Diode Effect without Magnetic Order in Polar $FeZnMo_3O_8$, Phys. Rev. Lett. **120**, 037601 (2018).

19. T. Kurumaji, Y. Takahashi, J. Fujioka, R. Masuda, H. Shishikura, S. Ishiwata, and Y. Tokura, Optical Magnetoelectric Resonance in a Polar Magnet (Fe, Zn)$_2$Mo$_3$O$_8$ with Axion-Type Coupling, Phys. Rev. Lett. **119**, 077206 (2017).
20. N. D. Khanh, N. Abe, H. Sagayama, A. Nakao, T. Hanashima, R. Kiyanagi, Y. Tokunaga, and T. Arima, Magnetoelectric coupling in the honeycomb antiferromagnet Co$_4$Nb$_2$O$_9$, Phys. Rev. B **93**, 075117 (2016).
21. V. Caignaert, A. Maignan, K. Singh, Ch. Simon, V. Pralong, B. Raveau, J. F. Mitchell, H. Zheng, A. Huq, and L. C. Chapon, Gigantic magnetic-field-induced polarization and magnetoelectric coupling in a ferrimagnetic oxide CaBaCo$_4$O$_7$, Phys. Rev. B **88**, 174403 (2013).
22. Y. Tokunaga, N. Furukawa, H. Sakai, Y. Taguchi, T. Arima, and Y. Tokura, Composite domain walls in a multiferroic perovskite ferrite, Nat. Mater. **8**, 558 (2009).
23. Y. S. Oh, S. Artyukhin, J. J. Yang, V. Zapf, J. W. Kim, D. Vanderbilt, and S.-W. Cheong, Non-hysteretic colossal magnetoelectricity in a collinear antiferromagnet, Nat. Commun. **5**, 3201 (2014).
24. F. A. Cotton, Metal Atom Clusters in Oxide Systems, Inorg. Chem. **3**, 1217 (1964).
25. H. Abe, A. Sato, N. Tsujii, T. Furubayashi, M. Shimoda, Structural refinement of T_2Mo$_3$O$_8$ (T= Mg, Co, Zn and Mn) and anomalous valence of trinuclear molybdenum clusters in Mn$_2$Mo$_3$O$_8$, J. Solid State Chem. **183**, 379 (2010).
26. S. Nakayama, R. Nakamura, M. Akaki, D. Akahoshi, and H. Kuwahara, Ferromagnetic Behavior of (Fe$_{1-y}$Zn$_y$)$_2$Mo$_3$O$_8$ ($0 \leq y \leq 1$) Induced by Nonmagnetic Zn Substitution, J. Phys. Soc. Jpn. **80**, 104706 (2011).
27. S. P. McAlister and P. Strobel, Magnetic order in M$_2$Mo$_3$O$_8$ single crystals (M=Mn, Fe, Co, Ni), J. Magn. Magn. Mater. **30**, 340 (1983).
28. J. R. Morey, A. Scheie, J. P. Sheckelton, C. M. Brown, and T. M. McQueen, Ni$_2$Mo$_3$O$_8$: Complex antiferromagnetic order on a honeycomb lattice, Phys. Rev. Mater. **3**, 014410 (2019).

29. D. Bertrand, H. Kerner-Czeskleba, Étude structurale et magnétique de molybdates d'éléments de transition, J. Phys. France, **36**, 379 (1975).

30. P. Strobel and Y. L. Page, Growth and morphology of single crystals of hexagonal molybdates (IV) $M_2Mo_3O_8$ (M = Mn, Fe, Co, Ni), J. Cryst. Growth **61**, 329 (1983).

31. P. Strobel, Y. L. Page, and S. P. Mcalister, Growth and physical properties of single crystals of $Fe^{II}{}_2Mo^{IV}{}_3O_8$, J. Solid State Chem. **42**, 242 (1982).

32. V. Petricek, M. Dusek, and L. Palatinus, Crystallographic Computing System JANA2006: General features, Z. Kristallogr. **229**, 345 (2014).

33. J. Bergmann, R. Kleeberg, A. Haase, and B. Breidenstein, Advanced Fundamental Parameters Model for Improved Profile Analysis, Mat. Sci. Forum, **347-349**, 303 (2000).

34. L. Lin, H. X. Zhu, X. M. Jiang, K. F. Wang, S. Dong, Z. B. Yan, Z. R. Yang, J. G. Wan, and J.-M. Liu, Coupled ferroelectric polarization and magnetization in spinel $FeCr_2S_4$, Sci. Rep. **4**, 6530 (2014).

35. S. S. P. Parkin and R. H. Friend, 3*d* transition-metal intercalates of the niobium and tantalum dichalcogenides. I. Magnetic properties, Phil. Mag. B **41**, 65 (1980).

36. S. J. Joshua, Power-law form of the temperature dependence of the magnon specific heat $C_M(T)$ in linear, planar and spatial antiferromagnets, Aust. J. Phys, **37**, 305 (1984).

37. B. J. Campbell, H. T. Stokes, D. E. Tanner, and D. M. Hatch, ISODISPLACE: a web-based tool for exploring structural distortions, J. Appl. Cryst. **39**, 607 (2006).

38. A. Maignan and C. Martin, $Fe_4Nb_2O_9$: A magnetoelectric antiferromagnet, Phys. Rev. B **97**, 161106(R) (2018).

39. D. Niermann, C.□P. Grams, P. Becker, L. Bohatý, H. Schenck, and J. Hemberger, Critical Slowing Down near the Multiferroic Phase Transition in $MnWO_4$, Phys. Rev. Lett. **114**, 037204 (2015).

40. V. A. Trepakov, O. E. Kvyatkovskii, M. E. Savinov, A. Dejneka, X. Wang, and S.-W. Cheong, Features of the low-frequency polarization response in the region of the ferroelectric phase transition in multiferroic $TbMnO_3$, Phys. Sol. State **58**, 2021 (2016).

41. S. V. Gallego, J. Etxebarria, L. Elcoro, E. S. Tasci, and J. M. Perez-Mato, Automatic calculation of symmetry-adapted tensors in magnetic and non-magnetic materials: a new tool of the Bilbao Crystallographic Server, Acta Crystallogr A **75**, 438 (2019).

TABLE I. Refined structure parameters of polycrystalline $Co_2Mo_3O_8$ from powder neutron diffraction data measured at 300 K.

Cell parameters	a(Å)	b(Å)	c(Å)	α	β	γ	Space group
	5.7698(1)	5.7698(1)	9.9134(1)	90	90	120	$P6_3mc$

Atom	x	y	z	Occ.	B_{iso}
Co1	0.33333	0.66667	0.9478(3)	1	0.29(3)
Co2	0.33333	0.66667	0.5116(2)	1	0.01(3)
Mo1	0.1460(1)	0.8540(1)	0.2494(1)	1	0.099(6)
O1	0.00000	0.00000	0.3913(1)	1	0.227(16)
O2	0.33333	0.66667	0.1457(1)	1	0.181(17)
O3	0.4879(1)	0.5121(6)	0.3649(1)	1	0.231(8)
O4	0.1673(1)	0.8327(1)	0.6331(1)	1	0.306(8)

TABLE II. Refined structure parameters of polycrystalline $Co_2Mo_3O_8$ from powder neutron diffraction data measured at 10 K.

Cell parameters	a(Å)	b(Å)	c(Å)	α	β	γ	Space group
	5.7658(3)	5.7658(3)	9.9053(0)	90	90	120	$P6_3mc$

Atom	x	y	z	Occ.	B_{iso}
Co1	0.33333	0.66667	0.9488(1)	1	0.010*
Co2	0.33333	0.66667	0.5122(4)	1	0.010*
Mo1	0.1461(1)	0.8538(9)	0.2496(3)	1	0.010*
O1	0.00000	0.00000	0.3918(3)	1	0.098
O2	0.33333	0.66667	0.1455(3)	1	0.083
O3	0.4876(8)	0.5123(2)	0.3654(2)	1	0.050
O4	0.16730	0.83270	0.6331(3)	1	0.105

*The displacement parameters were fixed at 0.01 Å^2 during the refinement.

TABLE III. List of the magnetic space groups generated using the ISODISTORT, using parent space group $P6_3mc$ with $\boldsymbol{k} = (0, 0, 0)$, for the 10 K dataset of $Co_2Mo_3O_8$.

IR	Magnetic S.G	S.G. number	moment along c (in the order of TTOO)	in-plane moment allowed?
mGM2	$P6_3m'c'$	186.207	++--	No
mGM3	$\boldsymbol{P6_3'm'c}$	**186.205**	**+-+-**	**No**
	$Cmc2_1$	36.172	0000	Yes
mGM5	$Cm'c'2_1$	36.176	++--	Yes
	$P2_1$	4.7	++--	Yes
	$Cmc'2_1'$	36.175	0000	Yes
mGM6	$Cm'c2_1'$	36.174	+-+-	Yes
	$P2_1'$	4.9	+-+-	Yes

Captions of figures

Fig. 1. (a) Crystal structure of $A_2Mo_3O_8$ (A: Mn, Fe, Co and Ni). A (OCT) and A (TET) represent the octahedral and tetrahedral coordination of magnetic atoms, respectively. (b) The schematic diagram of antiferromagnetic order in $Fe_2Mo_3O_8$. (c) Ferrimagnetic order in $Mn_2Mo_3O_8$.

Fig. 2. (a) Temperature dependence of the magnetic susceptibility $\chi(T)$ and Curie-Weiss fitting ($1/\chi$). (b) Magnetic field dependence of the magnetization $M(H)$ under selected temperatures.

Fig. 3. (a) T dependence of specific heat $C_P(T)$ of magnetic $Co_2Mo_3O_8$ and nonmagnetic $Zn_2Mo_3O_8$. Red curve represents magnetic specific heat (C_M), calculated by subtracting the C_P of $Zn_2Mo_3O_8$ from that of $Co_2Mo_3O_8$. (b) Temperature dependence of magnetic entropy $\Delta S_M(T)$. (c) The C_M-T curves under different magnetic fields.

Fig. 4. Rietveld fit of the NPD patterns measured at (a) 300 K, (b) 50 K, and (c) 10 K respectively. The inset shows the zoomed view of a selected reflection (100) at T=50 K and 10 K.

Fig. 5. The sketch of collinear magnetic order refined from the NPD data. The red and green colored arrows denote the magnetic moment on Co1 and Co2 sites.

Fig. 6. (a) Temperature dependence of dielectric constant $\varepsilon(T)$ for selected frequencies. (b) $\varepsilon(T)$ curves under applying magnetic fields with f=63 kHz.

Fig. 7. (a) Temperature dependence of pyroelectric currents $I_{py}(T)$ measured under different heating rates. The inset shows the electric polarization (P) under positive and negative

pooling electric field under 4 K/min heating rate. (b) The relationship of T dependence of $I_{py}(T)$ under different H. (c) The time-integrated change of electric polarization $P(T)$ under different H. (d) The measured H-dependent pyrocurrent I under $T = 30$ K.

Fig. 8. The XRD pattern of as-grown single crystal (hexagonal plate). The inset shows the image and Laue spots of the crystal.

Fig. 9. (a) The T-dependent pyroelectric current I_c and polarization P_c along the c axis for the single crystal. (b) H dependence of M along c-axis under $H//c$ and $H \perp c$. (c) H dependence of polarization ΔP_c measured at different temperatures under $H//c$. The dashed line is the fit to the ΔP_c-H curve with the function of $\Delta P = \beta H^2$, where β is constant. (d) The T dependence of β under $H//c$.

Fig. 10. Schematics of all ionic displacement in a unit cell upon transition from PM to AFM state in $Co_2Mo_3O_8$.

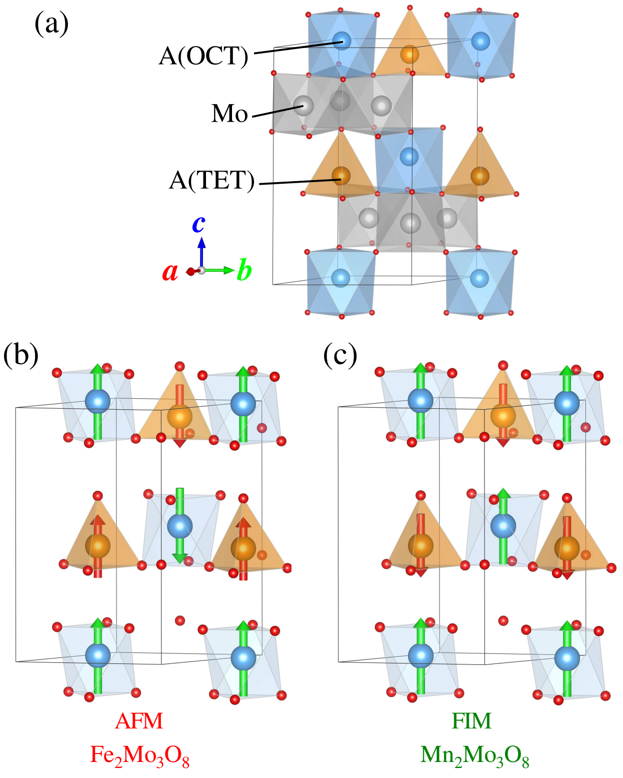
(a)
A(OCT)
Mo
A(TET)
c
a
b
(b)
(c)
AFM
$Fe_2Mo_3O_8$
FIM
$Mn_2Mo_3O_8$

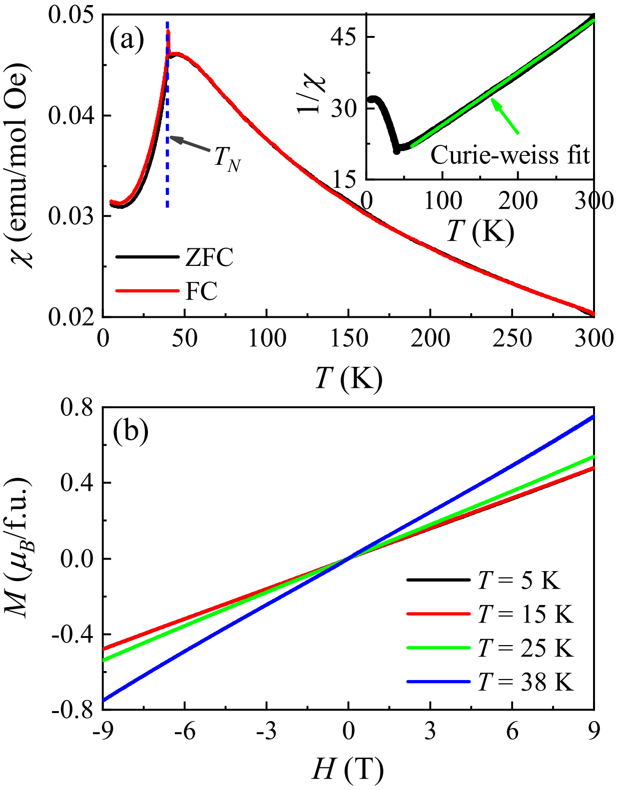
(a)
χ (emu/mol Oe)
0.05
0.04
0.03
0.02
T_N
ZFC
FC
0
50
100
150
200
250
300
T (K)
$1/\chi$
45
30
15
0
100
200
300
T (K)
Curie-weiss fit
(b)
M (μ_B/f.u.)
0.8
0.4
0.0
-0.4
-0.8
T = 5 K
T = 15 K
T = 25 K
T = 38 K
-9
-6
-3
0
3
6
9
H (T)

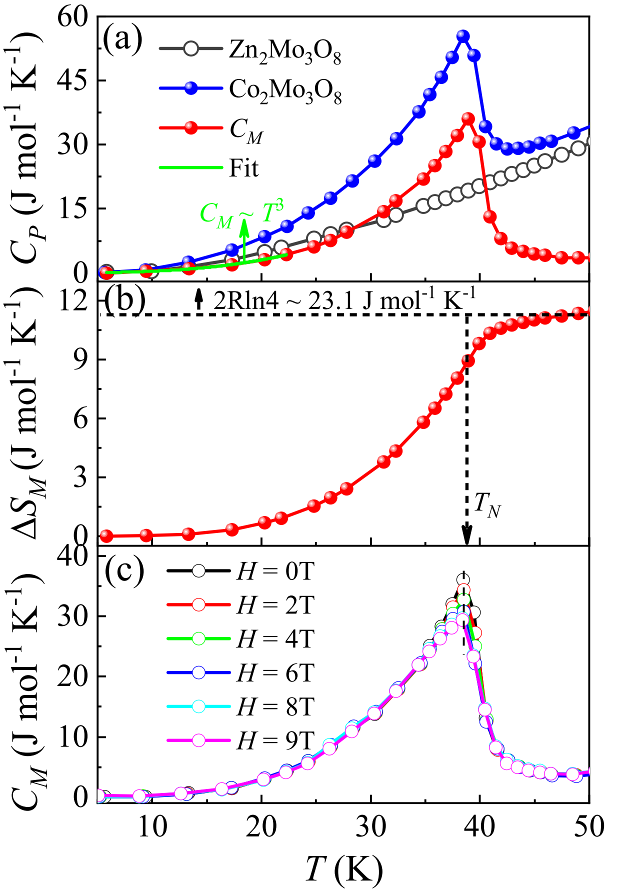
(a)
Zn2Mo3O8
Co2Mo3O8
C_M
Fit
C_M ~ T^3
C_P (J mol^-1 K^-1)
60
45
30
15
0
(b)
2Rln4 ~ 23.1 J mol^-1 K^-1
ΔS_M (J mol^-1 K^-1)
12
9
6
3
0
T_N
(c)
H = 0T
H = 2T
H = 4T
H = 6T
H = 8T
H = 9T
C_M (J mol^-1 K^-1)
40
30
20
10
0
10
20
30
40
50
T (K)

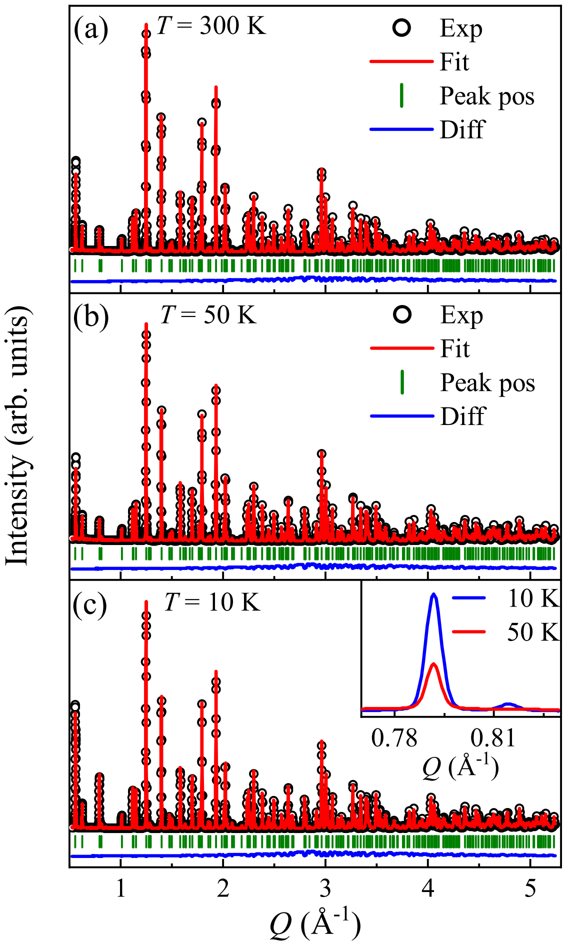
(a)
T = 300 K
Exp
Fit
Peak pos
Diff
(b)
T = 50 K
Exp
Fit
Peak pos
Diff
(c)
T = 10 K
10 K
50 K
0.78
0.81
Q (Å^{-1})
Intensity (arb. units)
1
2
3
4
5
Q (Å^{-1})

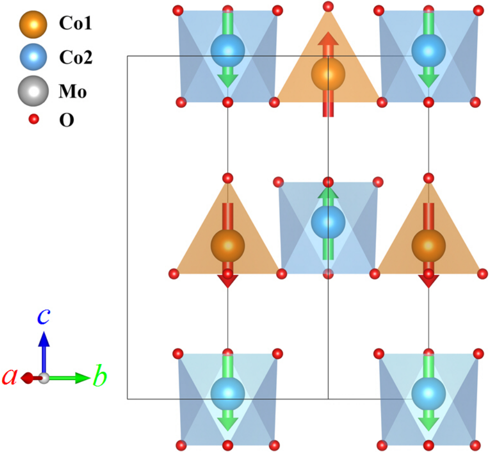
Co1
Co2
Mo
O
c
a
b

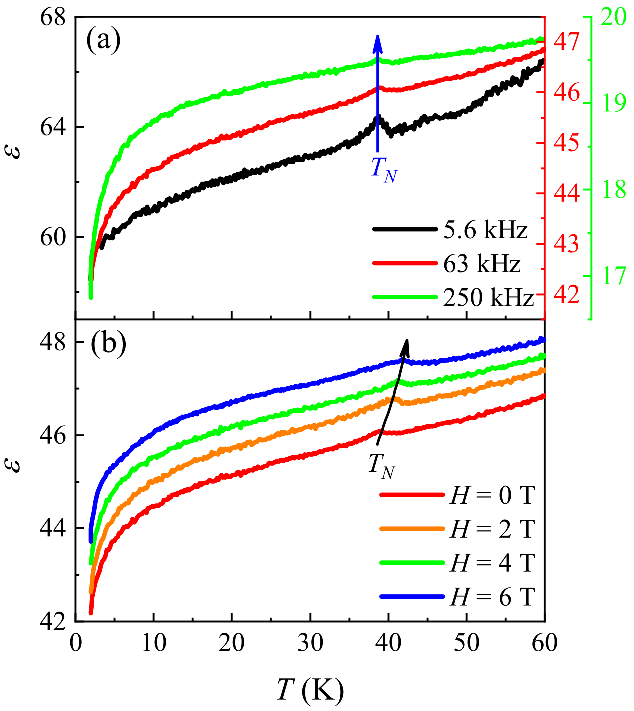
(a)
68
64
60
ε
47
46
45
44
43
42
20
19
18
17
T_N
5.6 kHz
63 kHz
250 kHz
(b)
48
46
44
42
ε
T_N
H = 0 T
H = 2 T
H = 4 T
H = 6 T
0
10
20
30
40
50
60
T (K)

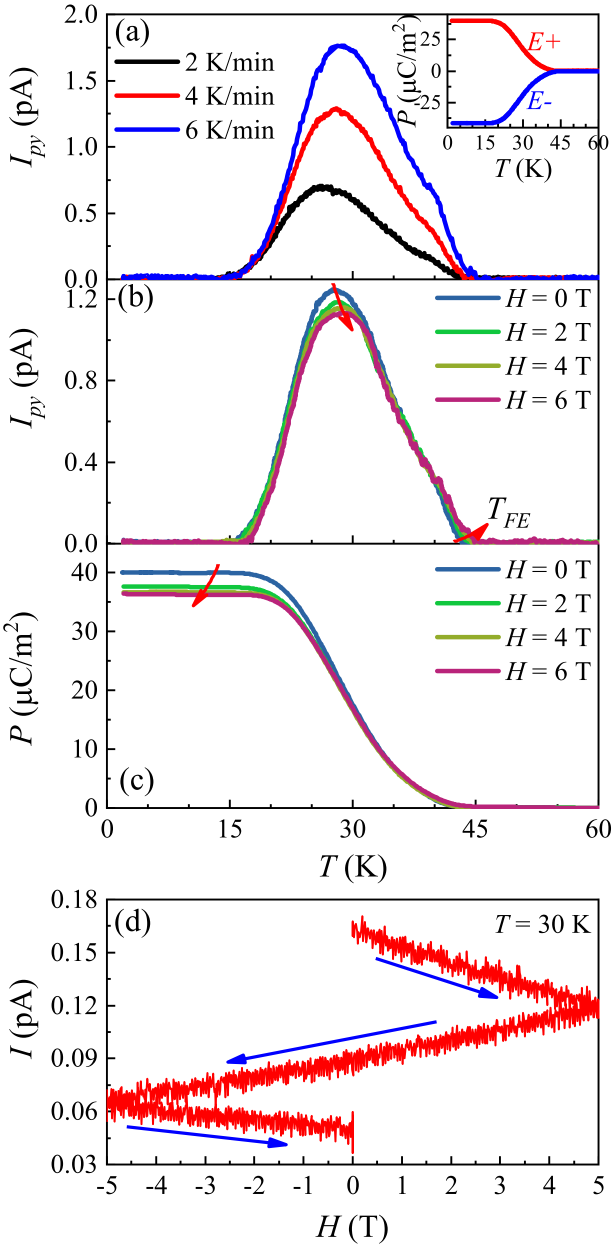
(a)
2 K/min
4 K/min
6 K/min
I_{py} (pA)
2.0
1.5
1.0
0.5
0.0
P (μC/m^2)
25
0
-25
0
15
30
45
60
T (K)
$E+$
$E-$
(b)
I_{py} (pA)
1.2
0.8
0.4
0.0
H = 0 T
H = 2 T
H = 4 T
H = 6 T
T_{FE}
(c)
P (μC/m^2)
40
30
20
10
0
H = 0 T
H = 2 T
H = 4 T
H = 6 T
0
15
30
45
60
T (K)
(d)
T = 30 K
I (pA)
0.18
0.15
0.12
0.09
0.06
0.03
-5
-4
-3
-2
-1
0
1
2
3
4
5
H (T)

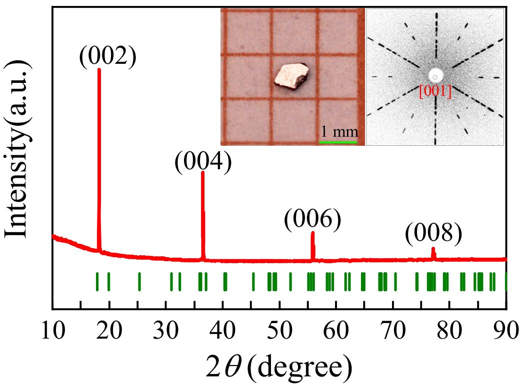
(002)
(004)
(006)
(008)
1 mm
[001]
Intensity(a.u.)
10
20
30
40
50
60
70
80
90
2θ (degree)

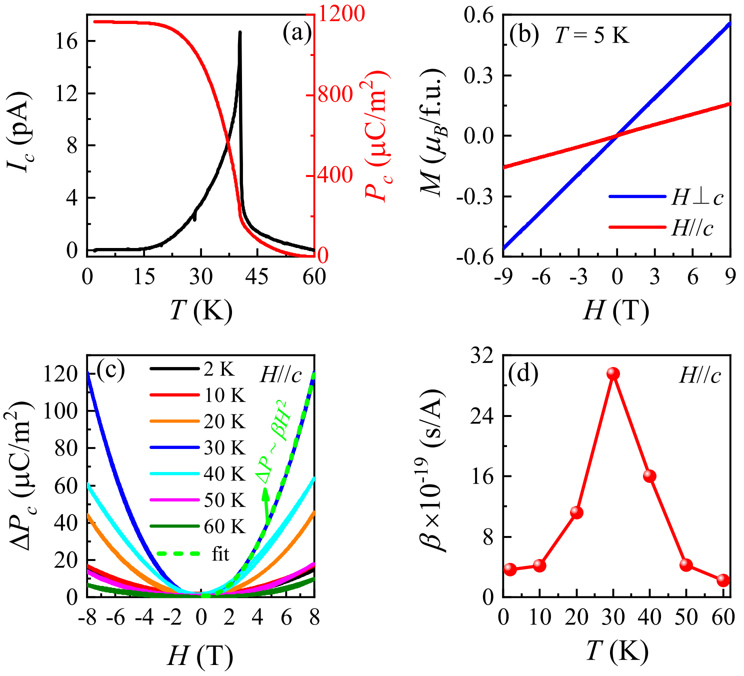
(a)
I_c (pA)
P_c (μC/m^2)
T (K)
0
4
8
12
16
400
800
1200
15
30
45
60
(b)
T = 5 K
M (μ_B/f.u.)
H (T)
$H \perp c$
$H//c$
0.6
0.3
0.0
-0.3
-0.6
-9
-6
-3
0
3
6
9
(c)
$H//c$
2 K
10 K
20 K
30 K
40 K
50 K
60 K
fit
$\Delta P \sim \beta H^2$
ΔP_c (μC/m^2)
H (T)
0
20
40
60
80
100
120
-8
-6
-4
-2
0
2
4
6
8
(d)
$H//c$
$\beta \times 10^{-19}$ (s/A)
T (K)
0
8
16
24
32
0
10
20
30
40
50
60

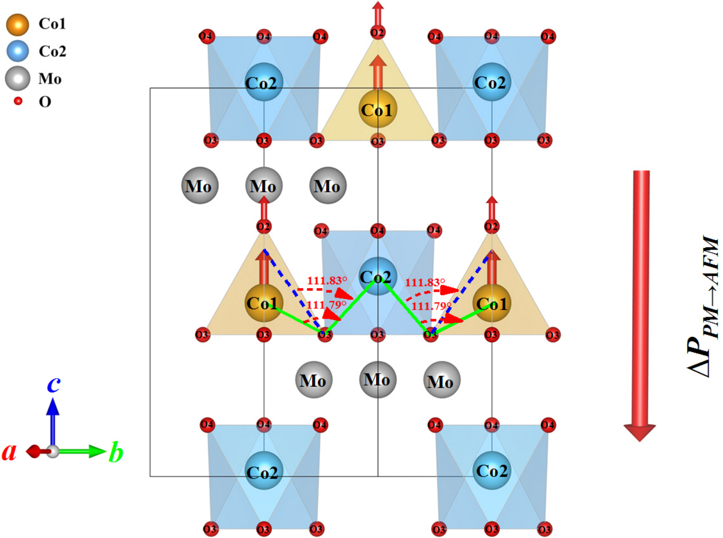
Co1
Co2
Mo
O
O4
O2
O3
111.83°
111.79°
c
a
b
$\Delta P_{PM\rightarrow AFM}$